

Energetics of C–N coupling reactions on Pt(111) and Ni(111) surfaces from application of density-functional theory†

Cite this: *Phys. Chem. Chem. Phys.*, 2013, **15**, 10395

Wei-Jia Chen, Chen-Hao Yeh, Chun-Chih Chang and Jia-Jen Ho*

We applied density-functional theory (DFT) with the projector-augmented-wave method (PAW) to investigate systematically the energetics of C–N coupling reactions on Pt(111) and Ni(111) surfaces. Our approach includes several steps: the adsorption of reactants and products (CH_x , NH_y and CH_xNH_y , $x = 0-3$, $y = 0-2$), movement of molecular fragments on the surface, and then C–N coupling. According to our calculations, the energies (ignoring the conventional negative sign) of adsorption of CH_x and NH_y on Pt(111)/Ni(111) surfaces decrease in the order $\text{C} > \text{CH} > \text{CH}_2 > \text{CH}_3$ and $\text{N} > \text{NH} > \text{NH}_2$, with values 7.41/6.91, 6.97/6.52, 4.58/4.39, 2.19/2.01 eV and 5.10/5.49, 4.12/4.79, 2.75/2.87 eV, respectively. Regarding the adsorption energies among CH_xNH_y , the adsorption energy of CNH_2 species is the highest on the Pt(111) surface, whereas on the Ni(111) surface CH_3N is the most stable. The C–N coupling barriers differ on the two metallic surfaces despite the structures of initial, transition and final states being similar. On the Pt(111) surface, the coupling reaction of $\text{CH}_2 + \text{NH}_2$ has the smallest barrier, whereas $\text{CH} + \text{NH}_2$ is the most favorable on the Ni(111) surface. The detailed local density of states (LDOS) and electron-localization functions (ELF) were investigated to rationalize the calculated outcomes.

Received 20th February 2013,
Accepted 22nd April 2013

DOI: 10.1039/c3cp50765c

www.rsc.org/pccp

1. Introduction

The C–N coupling reaction on a metallic surface is an important catalytic process in the industrial synthesis of hydrogen cyanide (HCN), a chemical intermediate in the production of dyes, medicines, nylon-66, *etc.*¹ In the synthesis of hydrogen cyanide two familiar processes involve the introduction of methane and ammonia at a temperature of ~ 1500 K over platinum catalysts. The Andrussov process,² $2\text{CH}_4 + 2\text{NH}_3 + 3\text{O}_2 \rightarrow 2\text{HCN} + 6\text{H}_2\text{O}$,

is strongly exothermic by 556 kJ mol^{-1} in the presence of oxygen, whereas in the absence of oxygen the Degussa process,³ $\text{CH}_4 + \text{NH}_3 \rightarrow \text{HCN} + 3\text{H}_2$, is endothermic by 255 kJ mol^{-1} . Various mechanisms of such a synthesis of hydrogen cyanide have been proposed on the basis of experimental and computational work.^{4–10} Herceg and Trenary^{4,5} reported that, after complete dehydrogenation of ammonia and methane on a Pt(111) surface, atomic C and N combine to form CN and hydrogenate to form HCN. Based on experiments Delagrè and Schuurman⁶ mentioned that the most probable reaction path for the synthesis of HCN is through hydrogenation of adsorbed CN on platinum catalysts, whereas Schmidt and Hickman⁷ proposed that this formation involved stepwise dehydrogenation of methylenimine (CH_2NH) and methylamine (CH_3NH_2) that are formed from fragments of ammonia and methane on a Pt supported catalyst. The experiments of Kondratenko *et al.*^{8,9} showed that, in the Andrussov process (with oxygen present), NO that was primarily formed *via* oxidation of ammonia reacted further with methane and ammonia to produce HCN and N_2 , respectively. Using density-functional theory, Gomez-Diaz and Lopez¹⁰ proposed that the presence of oxygen induced both direct $\text{C} + \text{N}$ and $\text{HC} + \text{N}$ couplings as the leading processes in the formation of HCN.

Department of Chemistry, National Taiwan Normal University, 88, Section 4, Tingchow Road, Taipei 116, Taiwan. E-mail: jjh@ntnu.edu.tw; Fax: +886-2-29324249; Tel: +886-2-29309085

† Electronic supplementary information (ESI) available. Table S1: the calculated adsorption energies (eV) for the different layers of the slab of atomic C on Pt(111) and Ni(111) surfaces. Fig. S1: local density of states (LDOS) for (a) N, (b) NH, and (c) NH_2 at the fcc hollow site on the Ni(111) surface. The blue, red and green lines represent the d orbital of top layer Ni atoms, s and p orbitals of the N atom and H atom, respectively. Fig. S2: local density of states (LDOS) for (a) C, (b) CH, (c) N, and (d) NH at the fcc hollow site on the Pt(111) surface. The blue and red lines represent the d orbital of top layer Pt atoms and s and p orbitals of the C(N) atom, respectively. Fig. S3: local density of states (LDOS) for (a) C, (b) CH, (c) N, and (d) NH at the fcc hollow site on the Ni(111) surface. The blue and red lines represent the d orbital of top layer Ni atoms and s and p orbitals of the C(N) atom, respectively. See DOI: 10.1039/c3cp50765c

From the above description, the synthesis of hydrogen cyanide in general may include adsorption and dehydrogenation of methane and ammonia, C–N coupling, dehydrogenation of CH_xNH_y , and desorption of HCN. However, the adsorption geometries, and the various C–N coupling mechanisms, presumed to be at the heart of the reactions, are still mysterious. The Pt(111) surface is generally used in industrial synthesis of hydrogen cyanide because of its great activity;^{11,12} nevertheless, it is quite costly. In our trial calculations, CH_x and NH_y on a Ni(111) surface exhibit greater adsorption energies than other surfaces, Cu and Pd, with the same fcc arrangement. Therefore, in this work we investigated the adsorption geometries of CH_x , NH_y and CH_xNH_y species with $x = 0\text{--}3$ and $y = 0\text{--}2$, as well as the barriers and reaction energies of coupling of $\text{CH}_x + \text{NH}_y$ on both Pt(111) and Ni(111) surfaces, and make a comparison.

2. Computational details

All present calculations were undertaken with density-functional theory (DFT) and the plane-wave method, utilizing the Vienna *ab initio* simulation package (VASP).^{13–17} We used the projector-augmented-wave method (PAW)^{18,19} in conjunction with the generalized gradient approximation (GGA) and Perdew–Wang 1991 (PW91)²⁰ exchange–correlation function. The calculations were performed with $(4 \times 4 \times 4)$ and $(4 \times 4 \times 1)$ Monkhorst–Pack²¹ mesh k -points for bulk and surfaces, respectively; a truncation energy of 400 eV was set with the convergence criterion 1×10^{-4} eV of total energy. The spin polarization calculation was only performed for the Ni system to take into account its ferromagnetic nature. The predicted lattice parameter of the Ni crystal, 3.52 Å, agrees satisfactorily with the experimental value,²² 3.51 Å, whereas that of Pt exceeds the experimental data²³ but by only 1.5%, indicating that the employed methods and models function properly in our system. We used a $p(3 \times 3)$ supercell for both Ni(111) and Pt(111) surfaces modeled as periodically repeating slabs with five layers, shown in Fig. 1(a) and (b). During the calculations the bottom two atomic layers were kept frozen whereas the remaining layers were fully relaxed. This surface model is justified by our further calculation listed in Table S1 (ESI†) such that the variation of

adsorption energies of atomic C on several surface models is less than 0.06 eV on both Pt and Ni surfaces.

The lateral cell of a Ni(111) surface has dimensions $a = b = 7.46$ Å and $c = 30$ Å; for a Pt(111) surface $a = b = 8.45$ Å and $c = 30$ Å, which includes a vacuum region of thickness greater than 20 Å to ensure no interaction between two slabs.

The adsorption energies were calculated according to the relation

$$E_{\text{ads}} = (E_{[\text{slab}]} + E_{[\text{adsorbate}]}) - E_{[\text{slab+adsorbate}]}$$

in which $E_{[\text{slab}]}$, $E_{[\text{adsorbate}]}$, and $E_{[\text{slab+adsorbate}]}$ are, respectively, the calculated electronic energies of a clean surface, a molecule in the gaseous phase, and species adsorbed on the surface. Vibrational wavenumbers of adsorbed structures were analyzed upon diagonalizing the Hessian matrix of selected atoms within the VASP approach. The nudged elastic-band (NEB) method^{24–26} was applied to locate transition states; the potential-energy surface (PES) was constructed accordingly. Frequency calculations were applied to these transition structures; only one imaginary frequency was obtained to confirm a transition state.

3. Results and discussion

3.1 Adsorption of reactants CH_x and NH_y

The energies of adsorption of CH_x ($x = 0\text{--}3$) and NH_y ($y = 0\text{--}2$) species at various sites on Pt(111) and Ni(111) surfaces are listed in Table 1. The monatomic species (C and N) show two stable locations – fcc hollow and hcp hollow sites – on these Pt(111) and Ni(111) surfaces with a η^3 configuration. The adsorption energies of the C atom at the fcc/hcp hollow sites are 7.41/7.30 eV and 6.86/6.91 eV on Pt(111) and Ni(111) surfaces, respectively, whereas for the N atom at fcc/hcp hollow sites the adsorption energies are 5.10/4.94 eV and 5.49/5.44 eV on Pt(111) and Ni(111) surfaces, respectively. CH and NH have similar adsorption structures at these fcc and hcp sites on these two surfaces. The computed energies of adsorption of CH are 6.97/6.88 eV and 6.52/6.50 eV at the fcc/hcp sites on Pt(111) and Ni(111) surfaces, respectively, and 4.12/3.89 eV and 4.79/4.69 eV, respectively, for NH species. CH_2 and NH_2 species favor moving to a bridge site to obtain a tetrahedral structure with adsorption energies of 4.58 and 2.75 eV, respectively, on the Pt(111) surface; CH_2 and NH_2 adsorbed at fcc hollow sites are preferable with adsorption

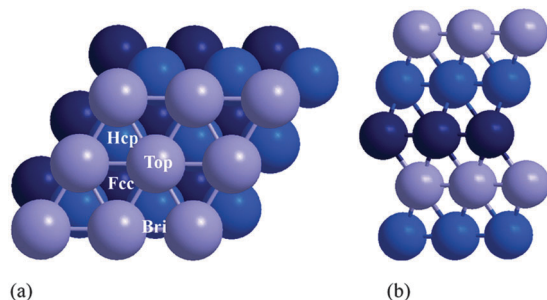


Fig. 1 Schematic presentation of a Pt(111) surface: (a) top view and (b) side view. The Ni(111) surface has the same structure as the Pt(111) surface. fcc, hcp, bri, and top represent fcc hollow, hcp hollow, bridge, and top sites, respectively.

Table 1 Adsorption energy/eV of CH_x ($x = 0\text{--}3$) and NH_y ($y = 0\text{--}2$) species at various sites on Pt(111) and Ni(111) surfaces. The bold font represents the most stable adsorption energy and the dashes indicate an unstable site

Species	Pt(111)/Ni(111)			
	Top	Bridge	hcp	fcc
N	—/—	—/—	4.94/5.44	5.10/5.49
NH	—/—	—/—	3.89/4.69	4.12/4.79
NH_2	2.13/2.15	2.75/2.86	—/2.86	—/2.87
C	—/4.47 ^a	—/6.55 ^a	7.30/6.86	7.41/6.91
CH	—/—	—/—	6.88/6.50	6.97/6.52
CH_2	3.68/3.27	4.58/—	—/4.38	—/4.39
CH_3	2.19/1.72	—/—	—/1.97	—/2.01

^a The x and y coordinates are fixed.

energies of 4.39 and 2.87 eV, respectively, on the Ni(111) surface. CH₃ shows three stable structures on the Ni(111) surface – a top site, a hcp hollow site and a fcc hollow site, with adsorption energies of 1.72, 1.97 and 2.01 eV, respectively; the fcc hollow site is hence the most stable. In contrast, we found only one stable adsorption site – the top site, with an adsorption energy of 2.19 eV on the Pt(111) surface.

According to these calculated data, we summarize the following points: (i) an increased number of hydrogen atoms of CH_x and NH_y species correlates with decreased adsorption energy on both surfaces; (ii) all NH_y species have larger adsorption energies on Ni(111) than on the Pt(111) surface, whereas all CH_x species have larger adsorption energies on Pt(111) than on the Ni(111) surface; (iii) since the energy differences between hcp and fcc sites for Ni(111) are very small, there is no clear preference for either the fcc or hcp site, whereas the species would be favorably adsorbed on the Pt(111) surface at various sites to saturate their coordination numbers, such as NH₂ being favorably adsorbed on the bridge site but CH₃ on the top site. (iv) For the species that can become adsorbed on both fcc and hcp hollow sites, the adsorption energies for the fcc hollow site indicate stronger binding on both surfaces. Although the adsorption of CH_x and NH_y species has been widely investigated on metallic surfaces,^{27–29} the electronic analysis of the above behaviors between the adsorbates and surfaces is unclear; in the following section we therefore apply local density of states and electronic localization functions to rationalize those interaction tendencies.

3.2 Analysis of electronic structure

Fig. 2(a)–(d) show the calculated local density of states (LDOS) of the surface metal d, carbon s and p, and hydrogen s orbitals, for CH_x species ($x = 0–3$) at fcc hollow sites on a Ni(111) surface, respectively. The integral overlap areas between surface metal (d orbital) and carbon (s and p orbitals) below the Fermi level are 0.89, 0.79, 0.71 and 0.50 for C, CH, CH₂, and CH₃ on the Ni(111) surface, respectively; the integral overlap areas between carbon

(s and p) and hydrogen s orbitals are 0, 0.17, 0.23 and 0.35. These values indicate that the strength of interaction between the carbon of CH_x and the surface decreases gradually and concurrently increases the interaction between carbon and hydrogen, resulting in gradually decreased binding energies 6.91, 6.52, 4.39 and 2.01 eV of C, CH, CH₂, and CH₃, respectively, on a Ni(111) surface. Similar LDOS are also discovered for NH_y ($y = 0–2$) species at fcc hollow sites on a Ni(111) surface shown in Fig. S1 (ESI[†]). The integral overlap areas between the metal d orbital and nitrogen (s and p) orbitals below the Fermi level are 1.16, 1.06, and 0.81 for N, NH, and NH₂, on the Ni(111) surface, respectively; the integral overlap areas between nitrogen (s and p) and hydrogen s orbitals are 0, 0.11, and 0.24, respectively. Such a smaller overlap magnitude representing weaker interaction between the adsorbates and the surface explains satisfactorily the above (i) phenomenon that an increasing number of hydrogen atoms of CH_x and NH_y species correlates with decreased adsorption energy on both surfaces.

Fig. S2 and S3 (ESI[†]) illustrate the LDOS of four adsorbates – C, CH, N and NH – at a fcc hollow site on Pt(111) and Ni(111) surfaces, respectively; Table 2 lists the integrated overlap areas between the metal d orbital and carbon (s and p)/nitrogen (s and p) orbitals below the Fermi level on both surfaces. The magnitudes of C and CH (1.01 and 0.96) on the Pt(111) surface are larger than those of Ni(111) (0.89 and 0.79), which indicates a stronger interaction between adsorbates and the Pt surface and results in greater binding energies of C and CH on Pt than on Ni surfaces. In contrast, for the N and NH species, binding energies are 1.11 and 0.99 on the Pt(111) surface, respectively, which are smaller than for the Ni(111) surface (1.16 and 1.04); smaller binding energies on Pt consequently appeared.

Fig. 3 shows electron-localization function³⁰ (ELF) contours of Pt(111) and Ni(111) surfaces. As shown for the Pt(111) surface in Fig. 3(a), the ELF value is distributed normally (gradually decreasing) from the nucleus (Pt) to its surroundings over the entire surface, which results in each adsorbed species locating in its most stable site correlating with the coordination number to attain a tetrahedral structure on the Pt(111) surface; for instance, the adsorbed CH₃ (that requires one further coordination to attain a tetrahedral structure) would sit at the top site of a Pt atom, and CH₂ at a bridge site (that requires two further coordinations), C and CH species at the hollow sites. On a Ni(111) surface, the ELF value is distributed differently with its greatest value at the fcc hollow site, leading to the greatest binding energies of all adsorbed species at the fcc hollow than at other sites.

Regarding the above (iv) calculated result, that the adsorption energy at the fcc hollow is invariably greater than that at the hcp hollow on both Pt and Ni surfaces for all adsorbed species clearly results from the ELF value for fcc hollow being still greater than for the hcp of both Pt(111) and Ni(111) surfaces.

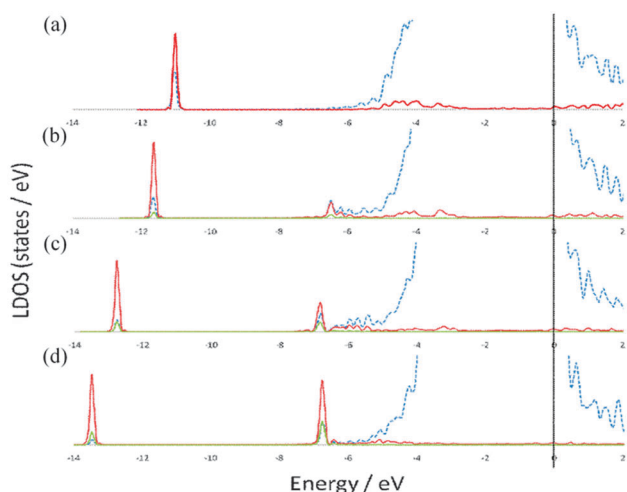


Fig. 2 Local density of states (LDOS) for (a) C, (b) CH, (c) CH₂ and (d) CH₃ at a fcc hollow site on a Ni(111) surface. The blue, red and green lines represent the d orbitals of top layer Ni atoms, s and p orbitals of the C atom and H atom, respectively.

Table 2 LDOS overlap (area unit) between the s and p orbitals of the C(N) atom and the d orbital of Ni atoms in the top layer of the surface

Surfaces	C	CH	N	NH
Pt(111) surface	1.01	0.96	1.11	0.99
Ni(111) surface	0.89	0.79	1.16	1.04

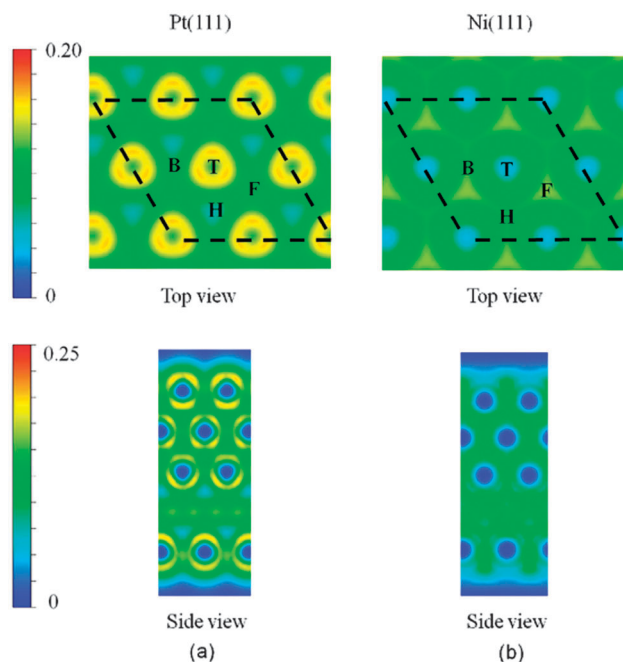


Fig. 3 Electron localization function contour map of the top and side views for (a) a Pt(111) surface and (b) a Ni(111) surface.

3.3 Adsorption of CH_xNH_y ($x = 0-3$, $y = 0-2$) on Pt(111) and Ni(111) surfaces

The calculated adsorption energies and geometric parameters of CH_xNH_y ($x = 0-3$, $y = 0-2$) species (possible products of C-N coupling reactions) on Pt(111) and Ni(111) surfaces are listed in Table 3. The CNH_y ($y = 0-2$) species (CN, CNH, and CNH_2) bind with the Pt(111) surface *via* their C atoms at a fcc hollow site in a $\eta^3(\text{C})$ mode (three coordinate) to satisfy the sp^3 hybridization of carbon atoms. Among these three CNH_y ($y = 0-2$) species, the CNH_2 has the greatest adsorption energy (4.99 eV) on the Pt(111) surface because the tetrahedral structures of both C and N atoms are satisfied for the adsorbed CNH_2 . HCN is adsorbed on a Pt(111) surface *via* its C and N atoms in a $\eta^2\eta^1$ mode with an adsorption energy of 0.97 eV and a C-N bond

length of 1.28 Å, the small adsorption energy is due to its octet structure. The preferable structure of CHNH adsorbed on a Pt(111) surface, *via* its C and N atoms bridging between two first-layer Pt atoms in a $\eta^1\eta^1$ mode, has an adsorption energy of 4.73 eV. The stable structure of CHNH_2 is adsorbed *via* its C and N atoms in a $\eta^2\eta^1$ mode on a Pt(111) surface with an adsorption energy of 3.09 eV and a C-N bond length of 1.47 Å. CH_2N and CH_2NH have similar configurations on the Pt surface, preferring to have their C and N atoms attached at top and bridge sites ($\eta^1\eta^2$ mode) of the Pt surface, with binding energies of 2.84 and 2.19 eV, respectively. Adsorbed CH_2NH_2 has a structure similar to that of CHNH, bridging between two first-layer Pt atoms in a $\eta^1\eta^1$ mode, with an adsorption energy of 3.09 eV on a Pt surface. CH_3N is adsorbed on a Pt(111) surface through its N atom as an N-end configuration (three coordinate) at the fcc hollow, with the CH_3 group pointing away from the surface and an adsorption energy of 4.51 eV; whereas CH_3NH is adsorbed *via* its N atom (two coordinate) at the bridge site (η^2 mode), with an adsorption energy of 2.38 eV; accordingly, CH_3NH_2 has its N atom attached on top of the Pt atom (an ethane-like structure) with the least adsorption energy of 1.07 eV. Similar adsorption structures of CH_xNH_y species were found on the Ni(111) surface with binding energies 4.10, 2.03, 4.63, 1.42, 4.31, 2.50, 3.11, 2.15, 2.47, 5.25, 3.21, 0.78 eV for CN, CNH, CNH_2 , HCN, CHNH, CHNH_2 , CH_2N , CH_2NH , CH_2NH_2 , CH_3N , CH_3NH , CH_3NH_2 , respectively.

3.4 The C-N coupling reactions

In Fig. 4(a)–(l), we describe the structures of the initial, transition, and final states for each C-N coupling reaction on the Pt(111) surface (similar structures were found for their Ni(111) counterparts); the detailed results for the activation barriers, reaction energies, and C-N distances of transition structures on both surfaces are listed in Table 4.

During the formation of a C-N bond with $\text{C} + \text{N}$ and $\text{C} + \text{NH}$ couplings shown in Fig. 4(a) and (b), each N-containing reactant gradually moves from its fcc hollow site toward another fcc hollow site at which the C atom is located, *via* a bridge location, to form the C-N bond on the surface. Unlike formation of CN and CNH, HCN is formed *via* the movement of the CH reactant towards the other N atom (Fig. 4(d)). The transition structures of the above three C-N coupling reactions – $\text{C} + \text{N}$, $\text{C} + \text{NH}$, and $\text{CH} + \text{N}$ – all locate at bridge sites on the surfaces with one reactant at the hollow site unmoved; the corresponding energy barriers are 1.44, 1.24 and 1.60 eV on the Pt(111) surface, whereas 1.26, 1.30 and 1.27 eV on Ni(111) respectively.

As shown in Fig. 4(g) and (h), the $\text{CH}_2 + \text{N}$ and $\text{CH}_2 + \text{NH}$ couplings have similar configurations of initial, transition, and final structures on the Pt(111) and Ni(111) surfaces. In the initial state, the N- and C-containing reactants are at fcc hollow and bridge sites, respectively; they then associate *via* C and N centers to form the transition structures, forming CH_2N and CH_2NH products with similar adsorption geometries ($\eta^1\eta^2$ (C, N)). Our calculated coupling energy barriers for $\text{CH}_2 + \text{N}$ and $\text{CH}_2 + \text{NH}$ are 1.12 and 1.01 eV on Pt(111), but 1.14 and 1.26 eV on Ni(111), respectively. Although the coupling of $\text{C} + \text{NH}_2$ and $\text{CH} + \text{NH}_2$

Table 3 Adsorption energy/eV and corresponding geometrical parameter/Å of C-N coupling products on the Pt(111) and Ni(111) surfaces (bri = bridge)

Pt(111)/Ni(111)					
Products	Site, mode	E_{ads}	$d_{\text{C-N}}$	$d_{\text{Pt(Ni)-C}}^a$	$d_{\text{Pt(Ni)-N}}^a$
CN	Fcc, $\eta^3(\text{C})$	4.13/4.10	1.20/1.19	2.16/1.99	
CNH	Fcc, $\eta^3(\text{C})$	1.98/2.03	1.25/1.24	2.06/1.93	
CNH_2	Fcc, $\eta^3(\text{C})$	4.99/4.63	1.36/1.34	2.03/1.87	
HCN	Bri, $\eta^2\eta^1(\text{C,N})$	0.97/1.42	1.28/1.31	2.21/2.01	2.00/1.94
CHNH	Bri, $\eta^1\eta^1(\text{C,N})$	4.73/4.31	1.29/1.30	1.97/1.85	2.05/1.88
CHNH_2	Bri, $\eta^2\eta^1(\text{C,N})$	3.09/2.50	1.47/1.47	2.04/1.90	2.13/1.98
CH_2N	Bri, $\eta^1\eta^2(\text{C,N})$	2.84/3.11	1.38/1.34	2.14/2.14	2.04/1.85
CH_2NH	Bri, $\eta^1\eta^2(\text{C,N})$	2.19/2.15	1.45/1.44	2.08/1.96	2.09/1.92
CH_2NH_2	Bri, $\eta^1\eta^1(\text{C,N})$	3.09/2.47	1.48/1.47	2.06/1.95	2.14/1.98
CH_3N	Fcc, $\eta^3(\text{N})$	4.51/5.25	1.46/1.46		2.06/1.84
CH_3NH	Bri, $\eta^2(\text{N})$	2.38/3.21	1.48/1.49		2.10/1.94
CH_3NH_2	Top, $\eta^1(\text{N})$	1.07/0.78	1.48/1.48		2.15/2.05

^a The values are average bond lengths.

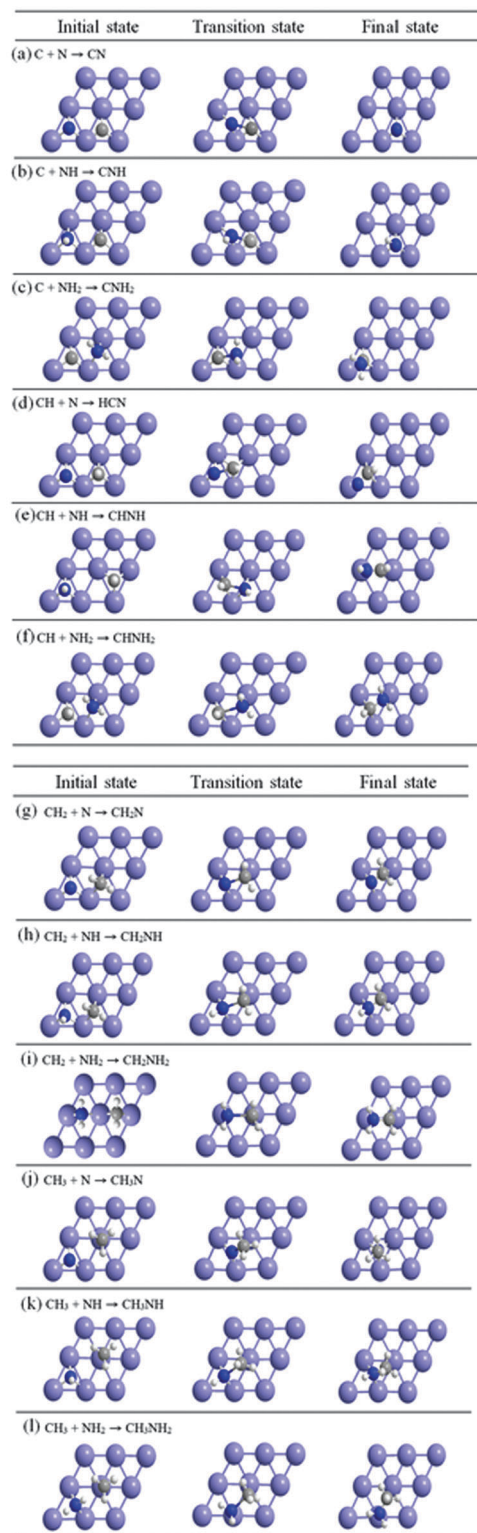


Fig. 4 Structures of initial, transition, and final states for the following coupling reactions: (a) $C + N$, (b) $C + NH$, (c) $C + NH_2$, (d) $CH + N$, (e) $CH + NH$, (f) $CH + NH_2$, (g) $CH_2 + N$, (h) $CH_2 + NH$, (i) $CH_2 + NH_2$, (j) $CH_3 + N$, (k) $CH_3 + NH$, and (l) $CH_3 + NH_2$.

had similar configurations for the initial states, different structures of transition and final states were found (Fig. 4(c) and (f)). For $C + NH_2$ coupling, C and NH_2 begin at fcc hollow and bridge

sites, and CNH_2 might be formed upon attaching the NH_2 to the C atom with reaction barriers of 1.00 and 0.94 eV on Pt and Ni surfaces, respectively. In contrast, for $CH + NH_2$ coupling, CH from the fcc hollow site gradually moves to a bridge site, forming $CHNH_2$ upon crossing the barriers of heights 1.01 and 1.18 eV on Pt and Ni surfaces, respectively. Among all coupling reactions, $C + NH_2$ is the most exothermic because the product CNH_2 has a stable tetrahedral structure.

$CHNH$ is formed *via* C and N centers, CH and NH , approaching each other from the hcp (CH) and fcc (NH) hollow sites, to produce the most stable $\eta^1\eta^1$ mode ($CHNH$) configuration, described in Fig. 4(e), with reaction barriers of 1.28 and 1.24 eV on Pt and Ni surfaces, respectively. In contrast to $CHNH$ formation, formation of CH_2NH_2 begins with coadsorbed CH_2 and NH_2 fragments, both at bridge sites of the surface (Fig. 4(i)). At the transition state, the CH_2 and NH_2 fragments stand perpendicularly at the top sites upon crossing the barriers of activation energies of 0.81 and 1.01 eV on Pt and Ni surfaces, respectively. For $CH_3 + N$ coupling on both surfaces shown in Fig. 4(j), the CH_3 and N atom first coadsorbed at top (CH_3) and fcc hollow (N) sites in the initial state; then the N atom moved from the fcc hollow to a bridge site whereas the CH_3 fragment from a top to a near-top site at the transition state with reaction barriers 1.33 and 0.90 eV on Pt and Ni surfaces, respectively. As shown in Fig. 4(k), a similar location of initial and transition structures was found for $CH_3 + NH$ coupling with reaction barriers of 1.45 and 1.19 eV on Pt and Ni surfaces, respectively. During the formation of CH_3NH_2 , the reactants, CH_3 and NH_2 fragments, begin at top and bridge sites, approaching each other (Fig. 4(l)); the $C-N$ bond shortens to 2.12 and 1.82 Å on Pt and Ni surfaces, respectively, with corresponding reaction barriers of 1.38 and 1.01 eV.

3.5 Discussion

The coupling reactions including CH_2 or NH_2 fragments, $CH_2 + N$, $CH_2 + NH$, $CH_2 + NH_2$, $C + NH_2$, and $CH + NH_2$, have small reaction barriers – 1.12, 1.01, 0.81, 1.00 and 1.01 eV – on a Pt(111) surface because the transition structures of these coupling reactions resemble those of the reactants, whereas, on a Ni(111) surface, the $N + CH_3$ and $C + NH_2$ coupling reactions have smaller barriers (0.90 and 0.94 eV) than the others. In contrast, the $C + N$, $CH + N$, and $C + NH$ coupling reactions are unfavorable with reaction barriers of 1.44, 1.60 and 1.24 eV on the Pt(111) surface whereas 1.26, 1.27 and 1.30 eV on the Ni(111) surface.

In some reports of experimental work the authors have shown that, as CH_4 and NH_3 were introduced into a Pt catalyst, HCN would be the only product at a high temperature, but according to our calculated results the formation of HCN from a direct $CH + N$ coupling is unfavorable, which indicates that the HCN might be produced from gradual dehydrogenation of a CH_xNH_y species; the surface HCN would become desorbed at a particular temperature. As a comparison of the barriers of $C-N$ coupling on the two surfaces, the barriers of $C-N$ coupling reactions on the Ni(111) surface are located in a range of smaller energies, 0.90–1.30 eV, than that for the Pt(111) counterparts, 0.81–1.60 eV. The Ni metal might hence be an alternative catalyst for HCN formation because of its low cost and high activity. Nevertheless, the reasons for the irregular

Table 4 Barrier, reaction energy, reaction free energy and C–N distance in the transition structures for C–N coupling reactions on Pt(111) and Ni(111) surfaces

Coupling reactions	Pt(111)/Ni(111)			
	E_a/eV	$\Delta E/\text{eV}$	ΔG (500 K)/eV	$d_{\text{C-N}}/\text{\AA}$
(a) $\text{C} + \text{N} \rightarrow \text{CN}$	1.44/1.26	−0.69/−0.75	−0.91/−0.96	1.89/1.87
(b) $\text{C} + \text{NH} \rightarrow \text{CNH}$	1.24/1.30	−1.09/−0.52	−1.08/−0.53	1.83/1.93
(c) $\text{C} + \text{NH}_2 \rightarrow \text{CNH}_2$	1.00/0.94	−1.55/−1.12	−1.45/−1.03	1.89/1.87
(d) $\text{CH} + \text{N} \rightarrow \text{HCN}$	1.60/1.27	0.09/−0.29	0.04/−0.25	1.77/1.97
(e) $\text{CH} + \text{NH} \rightarrow \text{CHNH}$	1.28/1.24	−0.25/0.50	−0.02/0.62	1.89/1.86
(f) $\text{CH} + \text{NH}_2 \rightarrow \text{CHNH}_2$	1.01/1.18	−0.33/0.05	−0.08/0.15	2.22/1.96
(g) $\text{CH}_2 + \text{N} \rightarrow \text{CH}_2\text{N}$	1.12/1.14	−0.33/−0.44	−0.24/−0.34	1.91/1.98
(h) $\text{CH}_2 + \text{NH} \rightarrow \text{CH}_2\text{NH}$	1.01/1.26	−0.41/−0.19	−0.22/−0.09	2.01/1.94
(i) $\text{CH}_2 + \text{NH}_2 \rightarrow \text{CH}_2\text{NH}_2$	0.81/1.01	−0.77/−0.14	−0.53/0.00	2.23/1.97
(j) $\text{CH}_3 + \text{N} \rightarrow \text{CH}_3\text{N}$	1.33/0.90	0.11/−0.39	0.14/−0.27	1.82/1.74
(k) $\text{CH}_3 + \text{NH} \rightarrow \text{CH}_3\text{NH}$	1.45/1.19	0.59/0.38	0.65/0.50	2.17/1.76
(l) $\text{CH}_3 + \text{NH}_2 \rightarrow \text{CH}_3\text{NH}_2$	1.38/1.01	−0.50/−0.24	−0.41/−0.19	2.12/1.82

differences of the activation energies of various C–N coupling reactions between these two surfaces are still unclear, and that would be another interesting topic in the future.

Conclusion

Using our calculations we systematically investigated the C–N coupling reactions on Pt(111) and Ni(111) surfaces, yielding information about the detailed local density of states (LDOS) and electron-localization function (ELF). Our results indicate the following points.

(i) The stabilities of CH_x and NH_y on Pt and Ni surfaces have the order $\text{C} > \text{CH} > \text{CH}_2 > \text{CH}_3$ and $\text{N} > \text{NH} > \text{NH}_2$, consistent with the order of integral overlap area of carbon (nitrogen) and surface being $\text{C} > \text{CH} > \text{CH}_2 > \text{CH}_3$ and $\text{N} > \text{NH} > \text{NH}_2$.

(ii) The N-containing species have greater adsorption energies on Ni(111) than on Pt(111) surfaces, whereas C-containing species behave oppositely.

(iii) The configurations of initial, transition and final structures in each coupling reaction are similar on Pt(111) and Ni(111) surfaces, with the transition states preferentially locating at a bridge or top site on the surfaces in each coupling reaction.

(iv) Among all C–N coupling reactions, $\text{CH}_2 + \text{NH}_2$ is the most favorable to proceed on a Pt(111) surface, whereas $\text{CH} + \text{NH}_2$ on a Ni(111) surface.

(v) According to the reaction barriers and reaction energies, the C–N coupling reactions on the Ni(111) surface could possess a similar catalytic reactivity to the Pt(111) surface. Consequently, the nickel surface would be a possible catalyst for the HCN formation reaction.

Acknowledgements

National Science Council of Republic of China (NSC 99-2113-M-003-007-MY3) supported this work; National Center for High-performance Computing provided computer time.

References

- C. N. Satterfield, *Heterogeneous Catalysis in Practice*, McGraw-Hill, New York, USA, 1980, p. 320.
- L. Andrussov, *Angew. Chem.*, 1935, **48**, 593–604.
- Kirk-Othmer *Encyclopedia of Chemical Technology*, ed. L. D. Pesce, Wiley, New York, USA, 2001, vol. 8, p. 171.
- E. Herceg and M. Trenary, *J. Am. Chem. Soc.*, 2003, **125**, 15758–15759.
- E. Herceg and M. Trenary, *J. Phys. Chem. B*, 2005, **109**, 17560–17566.
- S. Delagrangé and Y. Schuurman, *Catal. Today*, 2007, **121**, 204–209.
- L. D. Schmidt and D. A. Hickman, *Surface Chemistry and Engineering of HCN Synthesis, Catalysis of Organic Reactions*, Marcel-Dekker, New York, 1994, p. 195.
- V. A. Kondratenko, *Appl. Catal., A*, 2010, **381**, 74–82.
- V. A. Kondratenko, G. Weinberg, M. M. Pohl and D. S. Su, *Appl. Catal., A*, 2010, **381**, 66–73.
- J. Gomez-Diaz and N. Lopez, *J. Phys. Chem. C*, 2011, **115**, 5667–5674.
- L. Andrussov, *Ber. Dtsch. Chem. Ges.*, 1927, **60**, 536–540.
- L. Andrussov, *Production of Hydrocyanic Acid, U.S. Patent*, 1,934,838, 1930.
- G. Kresse and J. Hafner, *Phys. Rev. B: Condens. Matter Mater. Phys.*, 1993, **47**, 558–561.
- G. Kresse and J. Hafner, *Phys. Rev. B: Condens. Matter Mater. Phys.*, 1994, **49**, 14251–14269.
- G. Kresse and J. Hafner, *J. Phys.: Condens. Matter*, 1994, **6**, 8245–8256.
- G. Kresse and J. Furthmüller, *Comput. Mater. Sci.*, 1996, **6**, 15–50.
- G. Kresse and J. Hafner, *Phys. Rev. B: Condens. Matter Mater. Phys.*, 1996, **54**, 11169–11186.
- P. E. Blöchl, *Phys. Rev. B: Condens. Matter Mater. Phys.*, 1994, **50**, 17953–17979.
- G. Kresse and D. Joubert, *Phys. Rev. B: Condens. Matter Mater. Phys.*, 1999, **59**, 1758–1775.
- J. P. Perdew and Y. Wang, *Phys. Rev. B: Condens. Matter Mater. Phys.*, 1992, **45**, 13244–13249.
- H. J. Monkhorst and J. D. Pack, *Phys. Rev. B: Condens. Matter Mater. Phys.*, 1976, **13**, 5188–5192.
- V. Branger, V. Pelosin, K. Badawi and P. Goudeau, *Thin Solid Films*, 1996, **275**, 22–24.
- CRC Handbook of Chemistry and Physics*, ed. D. R. Lide, CRC Press, New York, USA, 76th edn, 1996.
- A. Ulitsky and R. Elber, *J. Chem. Phys.*, 1990, **92**, 1510–1512.

- 25 G. Mills, H. Jónsson and G. K. Schenter, *Surf. Sci.*, 1995, **324**, 305–337.
- 26 G. Henkelman, B. P. Uberuaga and H. Jónsson, *J. Chem. Phys.*, 2000, **113**, 9901–9904.
- 27 J. E. Mueller, A. C. T. Van Duin and W. A. Goddard, *J. Phys. Chem. C*, 2009, **113**, 20290–20306.
- 28 G. Novell-Leruth, A. Valcarcel, A. Clotet, J. M. Ricart and J. Perez-Ramirez, *J. Phys. Chem. B*, 2005, **109**, 18061–18069.
- 29 Y. Chen and D. G. Vlachos, *J. Phys. Chem. C*, 2010, **114**, 4973–4982.
- 30 A. D. Becke and K. E. Edgecombe, *J. Chem. Phys.*, 1990, **92**, 5397–5403.